



ELSEVIER

Materials Science and Engineering A360 (2003) 70–84

**MATERIALS
SCIENCE &
ENGINEERING**

A

www.elsevier.com/locate/msea

Phase, structural and microstructural investigations of plasma sprayed hydroxyapatite coatings

Limin Sun^{a,1}, Christopher C. Berndt^{a,*}, Clare P. Grey^b

^a Department of Materials Science and Engineering, Stony Brook University, Stony Brook, NY 11794-2275, USA

^b Department of Chemistry, Stony Brook University, Stony Brook, NY 11794-3400, USA

Received 14 March 2003; received in revised form 27 March 2003

Abstract

The properties and performance of plasma sprayed hydroxyapatite ($\text{Ca}_{10}(\text{PO}_4)_6(\text{OH})_2$, i.e. HA) coatings are closely related to their manufacturing process. The objective of the current study is to investigate the phase, structure and microstructure of the coatings and their formation mechanism due to different processing parameters. Hydroxyapatite powders were atmospherically plasma sprayed (APS) using various process parameters. The phase, structure and microstructure of the coatings were investigated and their microhardness measured. Both crystallinity and hydroxyl contents decreased with increasing spray power and stand-off distance (SOD), and increased from the coating interface to the surface. Crystallinity alone cannot reflect coating quality due to the existence of various forms of HA, i.e. unmelted, recrystallized and dehydroxylated, as well as the gradient structures consisting of these forms. Coating microstructure varied from a porous structure to a smooth glassy structure or a typical lamellar structure, and some newly formed nanocrystalline regions were revealed. These effects were associated with the temperature–time experiences of particles, their cooling rates and the heat and hydroxyl accumulation during coating buildup. The coating with highest recrystallization displayed the highest microhardness.

© 2003 Elsevier B.V. All rights reserved.

Keywords: Biomedical coatings; Thermal spray; Hydroxyapatite; Phase evolution; Recrystallization; Microstructural control

1. Introduction

Plasma spraying has been used as a major technique in applying hydroxyapatite ($\text{Ca}_{10}(\text{PO}_4)_6(\text{OH})_2$, HA) coatings onto metal implants to improve implant fixation and bone growth [1–3]. However, due to the extremely high temperature of the plasma flame and the rapid cooling rate, the phase and structure of the HA coatings are greatly changed from those of the feedstock. Variations in feedstock and deposition parameters can lead to different phase composition, crystal structure and microstructures [2,4,5], which result in the alterations of two major coating properties: mechanical

properties and dissolution behavior. For example, different phases have demonstrated different solubility [6,7] and Young's modulus [8]. Therefore, to obtain HA coatings with predictable properties and performance for implant application, the phase, structure and microstructure of the HA coatings should be designed for practical purposes. To achieve this, both the spray parameters and the feedstock HA should be optimally controlled.

Previous studies in this field usually reported on the coating crystallinity and its effects on the dissolution and mechanical property [2,9,10]. However, due to the existence of different forms of the crystalline HA; i.e. unmelted, recrystallized and dehydroxylated, and their variation within the coating, crystallinity alone may not reflect the coating quality. In addition, microstructural features such as the sub-microstructure, pores, cracks and splat boundaries also influence the coating quality, and these have seldom been investigated. In this study, highly crystalline HA powders were used as the feed-

* Corresponding author. Tel.: +1-631-632-8507; fax: +1-631-632-8525.

E-mail address: cberndt@notes.cc.sunysb.edu (C.C. Berndt).

¹ Present address: ADAF Paffenbarger Research Center, National Institute of Standards and Technology, 100 Bureau Drive, Stoa 8546, Gaithersburg, MD 20899-8546, USA.

stock. Phase, structure and microstructure of the HA coatings and their variations with the coating buildup were investigated with regard to the spray parameters. The aim is to improve the coating manufacture through the fundamental understanding of the relationship between the processing and coating characteristics.

2. Experimental

2.1. Feedstock and plasma spraying

The feedstock were calcined spray-dried HA powders, provided by the Advanced Materials Research Center (AMRC), Nanyang Technological University (NTU) of Singapore [11,121]. The powders are of highly crystallized pure HA phase and were sieved to less than 100 μm to ensure uniform melting and deposition for the spray process. The powders were then atmospherically plasma sprayed (APS) using a Metco 3 MB plasma torch with a GH nozzle (Sulzer-Metco, Westbury, NY, USA). Three spray power and two stand-off distances (SOD) were selected (Table 1). Argon was used as both the primary gas (at 50 slpm) and carrier gas (at 3.65 slpm), and hydrogen as the secondary gas. The transverse speed of the plasma gun was set at 300 mm s^{-1} . Air-cooling was used from the back of the substrate. Prior to spraying, the mild steel substrate was grit-blasted using Al_2O_3 and cleaned with acetone. Some substrates were lightly grit blasted to permit easy coating removal from the substrate after spraying. Coating thickness varied as a result of different spray passes and deposition efficiencies (DEs).

2.2. Characterization techniques

X-ray diffraction was performed on both the feedstock and the surface and interface (in the case of the peel-off coatings) of the coatings using a Philips PW 1729 X-ray diffractometer with $\text{CuK}\alpha_1$ radiation; the operating voltage was 40 kV and current 30 mA. The goniometer was set at a scan rate of $0.005^\circ \text{s}^{-1}$ over a 2θ range of $20\text{--}60^\circ$. Some coatings were gradually thinned

using abrasive paper and then measured using XRD to understand the phase variation during coating buildup. The crystallinity of the coatings was evaluated using the following equation, which was revised from some previous work [2,13–15]:

$$\text{Crystallinity (\%)} = \frac{A_C}{A_C + A_A} \times 100\% \quad (1)$$

where A_C is the total integrated intensity of all HA peaks in a 2θ range of $25\text{--}37^\circ$. It is calculated by multiplying the area of the most intensive (211) peak of the HA by a factor of 3.23, which is the ratio of the total intensity of all HA peaks within $25\text{--}37^\circ$ in JCPDS card (#9-432) to the intensity of the (211) peak. The term " A_A " is the integrated intensity of the ACP phase, which was evaluated using the area of the amorphous hump between 25 and 37° . All peak area calculations were performed using curve fitting and the relative error was estimated within $\pm 2\%$ of the mean value.

A Nicolet MAGNA-IR 760 spectrometer (Thermo Nicolet, Madison, WI, USA) was used to record the infrared spectra of the feedstock and coatings. Feedstock HA and four pulverized coatings were finely ground in the pestle and mortar, and then mixed with KBr at a weight ratio of $\sim 1:20$ and pressed into pellets. The spectra were acquired in the transmission mode over the range of $400\text{--}4000 \text{ cm}^{-1}$. In addition, both the surface and interface of the peel-off coatings were scanned in the reflective mode (i.e. the "diffuse reflection infra-red Fourier transform", DRIFT, technique) over the range of $700\text{--}4000 \text{ cm}^{-1}$.

Solid state ^{31}P MAS nuclear magnetic resonance (NMR) experiments were performed with a double-tuned Chemagnetics 4 mm probe on a Bruker 600 spectrometer (magnetic field of 14.1 T) at an operating frequency of 242.94 MHz and a spinning speed of 15 kHz, with pulse width of $2 \mu\text{s}$ ($\sim 60^\circ$) and delay of 6 s. The technique of magic angle spinning (MAS) was used to eliminate the effects of $^{31}\text{P}\text{--}^{31}\text{P}$ dipolar interactions and ^{31}P chemical shift anisotropy, so as to reduce signal broadening. The reference material was $(\text{NH}_4)\text{H}_2\text{PO}_4$, with $(\text{PO}_4)^{3-}$ at 0 ppm. The samples include feedstock HA, OHA (prepared by heat treating the HA powder at

Table 1
Plasma spray parameters

Sample ^a	Current (A)	Voltage (V)	H ₂ (slm)	Power (kW)	SOD (mm)
A1/A1p	500	55	5.6	27.5	80
A2/A2p	500	55	5.6	27.5	160
A3	500	70	11	35	80
A4	500	70	11	35	160
A5/A5p	600	70	11	42	80
A6/A6p	600	70	11	42	160

^a "p" refers to peel-off coating; i.e. a coating that was removed from the substrate so that analyzes could be performed on the back side of the sample, as well as porosity measurements.

900 °C in vacuum for 48 h) and four pulverized coatings. All powders were finely ground and then tightly packed into rotors.

The morphology of feedstock HA, coating surfaces and the cross-sectional microstructures of the coatings were examined using a LEO 1550 scanning electron microscope (SEM) and an optical microscope. The coatings were sectioned on a diamond cut-off wheel and mounted in epoxy resin under vacuum. The samples were then ground and polished, and 0.05 µm alumina was used for the final polishing step. All samples were made electrically conductive by coating with a thin layer of gold prior to the examination.

Microhardness tests were performed on the polished cross-section of the coatings using a Tukon Microhardness Tester (Instron, Canton, MA, USA). The load used was 50 gf and the load time was 15 s. The results were the average of 15 readings. The porosity of the coatings was measured with the peel-off coatings by using the Archimedian method.

3. Results and discussion

3.1. Phase analysis using XRD

3.1.1. Phase variations with spray parameters

Fig. 1 shows the XRD patterns of the HA coatings sprayed at different powers and SODs. At the same SOD, when the spray power increased, the overall intensity of HA peaks decreased and the amorphous hump became more obvious, especially for the SOD 160 mm case. Meanwhile, the peaks of all impurity phases (calcium phosphate ($\text{Ca}_3(\text{PO}_4)_2$, α -TCP, β -TCP), tetracalcium phosphate ($\text{Ca}_4\text{P}_2\text{O}_9$, TTCP) and calcium oxide (CaO)) also increased. On the other hand, at the same spray power, the intensity of all HA peaks decreased appreciably and the amorphous hump became significant when the SOD increased from 80 to 160 mm. The impurity peaks did not exhibit uniform change with increasing SOD (little change for TCP and TTCP peaks while obvious increase for CaO peak). In addition to the effects on the phase composition, when the SOD was increased from 80 to 160 mm, the deposition efficiency (DE, measured by the coating thickness per spray pass) was ~60% of the former. The change of spray power did not show any distinct influence on the DE.

The crystallinity of the HA coatings is shown in Fig. 2. The crystallinity decreased with increasing spray power and decreased significantly when the SOD increased from 80 to 160 mm. Due to the high temperature of the plasma flame, the HA particles will likely melt either wholly or partially. The melt could either (i) solidify to ACP, (ii) recrystallize, or (iii) decompose to impurity phases. In addition, the melt may be dehydroxylated and become OHA [6,16,17].

This dehydroxylation creates a barrier to the nucleation of the HA or OHA from the melt [18,19] and promotes the formation of the amorphous phase. The degree of both particle melting and dehydroxylation increased with the plasma temperature and their residence time in the plasma flame. The decomposition of the HA during the spray process can be explained using the related $\text{CaO-P}_2\text{O}_5\text{-H}_2\text{O}$ phase diagram [20] with the temperature–time exposure experiences of the HA particles and their cooling rate [21–23]. For example, at higher spray power, more HA powders melted and decomposed as the plasma temperature increased. Also the powders were more dehydroxylated, which could enhance the formation of impurity phases since the decomposition temperature decreased [20]. Since the impurity phases can be controlled to be very low by varying the feedstock and processing conditions [18], the current work will focus on the formation of amorphous and recrystallized phase.

The phase formation upon the droplet deposition depends on (i) both the hydroxyl state and the cooling rate of the droplet during the solidification process, and (ii) the heat/hydroxyl accumulation during coating buildup. A droplet can be viewed as a three-layered structure; i.e. unmelted core, stoichiometric melt interlayer and dehydroxylated melt shell, Fig. 3. This model is revised from some previous work [24,25] with the intent to investigate the recrystallization mechanisms in the plasma sprayed HA coating. It is assumed that a critical cooling rate exists such that the stoichiometric melt recrystallizes (path a in Fig. 3) while the dehydroxylated melt transforms to amorphous phase. The impurity phases were not considered for simplicity. Two pathways can lead to greater recrystallization; i.e. path b shows recrystallization of the dehydroxylated melt due to a decreased cooling rate, and path c indicates recrystallization of the amorphous phase in the prior-formed splat due to heat and hydroxyl accumulation during coating buildup. The substrate temperature can be in excess of 1000 °C (determined by the spray parameters) [26] due to the heat transfer from both the plasma flame and the droplets and this will decrease the cooling rate of the droplet. In addition, the heat accumulation may promote the recrystallization of the prior-formed amorphous phase in the coating since the recrystallization temperature of the amorphous phase has been reported to be 500–700 °C [15,24]. As well, since the time interval between the droplets covering the same spot of the substrate is as long as 0.1 s, about 10^6 -times the solidification time of the droplet (10^{-5} – 10^{-7} s) [18,24]; the prior-formed amorphous phase in the coating may incorporate hydroxyl from the surrounding air; i.e. the particle may be re-hydroxylated and promote the recrystallization of this portion of the splat. The re-hydroxylation usually happens at above 400 °C and increased with the temperature [15,24]. The experimen-

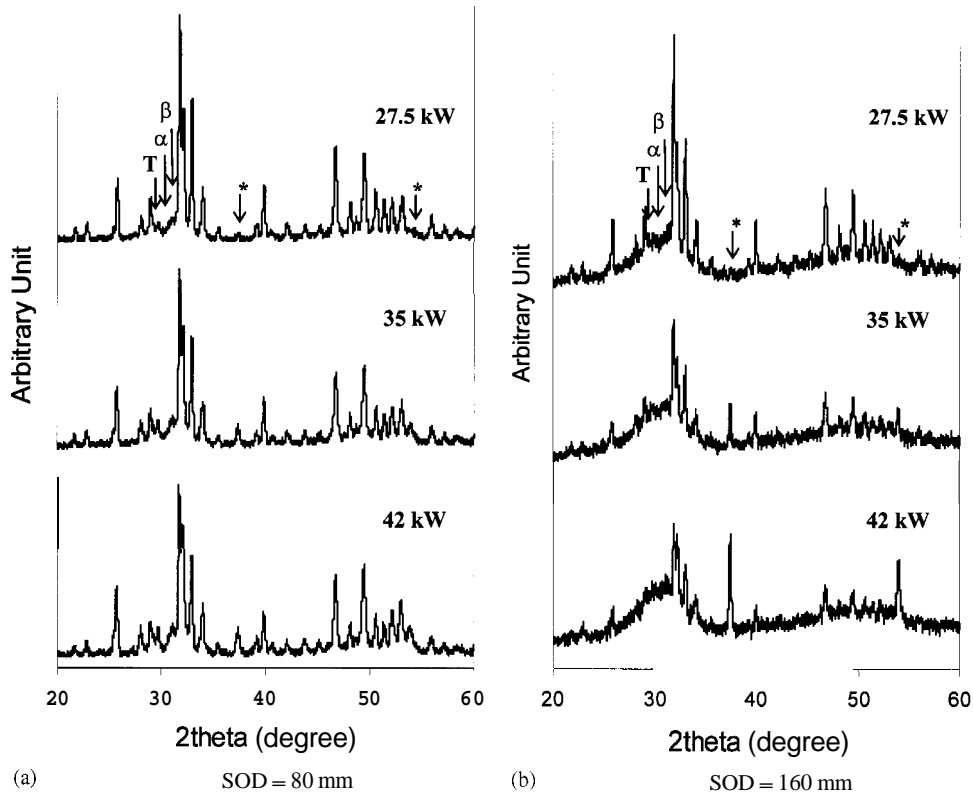


Fig. 1. XRD patterns of the HA coatings sprayed at different power and SOD. “ α ” is α -TCP, “ β ” is β -TCP, “T” is TTCP, “*” is CaO. All other peaks belong to HA.

tal evidence on this rehydroxylation process will be revealed later.

In this study, when the power increased from 27.5 to 42 kW, the temperature of both the plasma flame and the particle increased, therefore, there was more particle melting (dominant) and dehydroxylation, as stated before. In addition, the heat accumulation from both the flame and the incoming droplets increased, which

increased the substrate temperature, and, thus, decreased the cooling rate. This decreased cooling rate led to more recrystallization from the melt. The increased heat accumulation and re-hydroxylation also led to more recrystallization of the prior-formed amorphous phase. All these factors led to the higher ACP in the coating, and the crystalline HA phase consisted of more recrystallized components.

On the other hand, as the SOD increased from 80 to 160 mm; i.e. the substrate was further from the plasma flame, the HA particles suffered more dehydroxylation (the dominant phase change process, which is verified by FTIR as described later) and melting due to longer residence time. However, the substrate temperature greatly decreased in this case due to less heat accumulation from both the plasma flame and the arriving droplets whose temperature decreased with the longer residence time of the particles in the plasma flame. The much higher cooling rate inhibited the recrystallization of the dehydroxylated melt during the solidification process and, thus, much more ACP formed. In addition, as the temperature of both the substrate and the incoming droplets were lower, the recrystallization and rehydroxylation of the prior-formed amorphous phase in the coating also decreased. Another reason for the decrease of the crystallinity at longer SOD was the

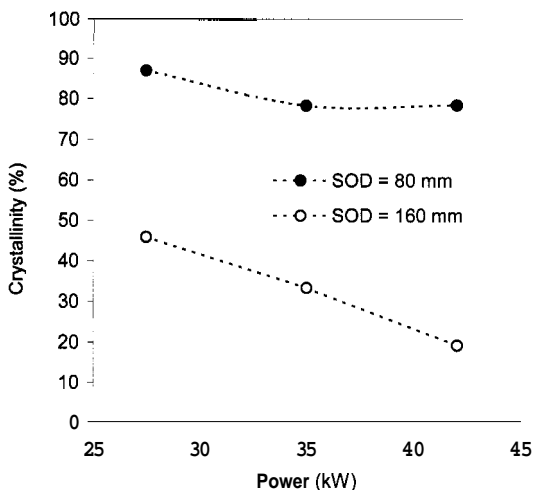


Fig. 2. Crystallinity of the HA coatings sprayed at different power and SOD.

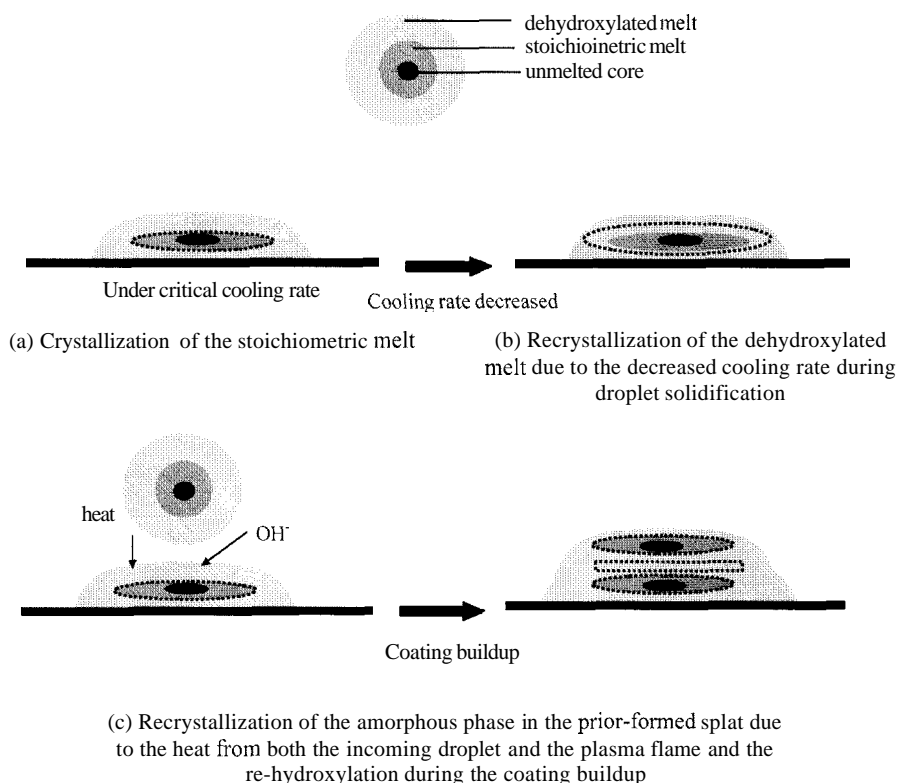


Fig. 3. Schematic diagram showing three recrystallization paths during droplet solidification (a, b) and coating buildup (c). (The dashed line separates the amorphous (outer) and recrystallized (inner) phases)

preferential loss of unmelted portions of the particles during spraying; i.e. some of the unmelted or partially melted particles were de-agglomerated and blown away before they impacted on the substrate or bounced away from the substrate. This phenomenon is evidenced by the SEM photos shown later as well as the fact that the deposition efficiency decreased around 40% when the SOD increased from 80 to 160 mm.

3.1.2. Phase variations in HA coatings

As shown in Fig. 4, in all four extreme spray power/SOD combinations, the intensity of the overall HA peaks is evidently lower while the amorphous hump is more obvious in the XRD patterns of the interface than that of the coating surface. For the impurity phases, the CaO peak (indicated with a “**”) is higher in the XRD pattern of the interface, while the peaks of TCP and TTCP are lower; possibly due to the more pronounced amorphous hump. The XRD pattern along the coating thickness (Fig. 5) displayed an internal gradient structure from an amorphous base to a crystalline surface. No obvious difference was found when the coating thickness exceeds 60 μm . Since the thickness of the HA coatings in clinical use (especially for the femoral stem) is usually around 50 μm , this gradient phase structure is expected to affect the coating properties and performance.

Fig. 6 compares the crystallinity between the coating surface and interface. The crystallinity was significantly lower at the coating interface in all four cases. This result is consistent with previous studies [24,27]. During the spray process, the cooling rate of the first lamella is controlled by rapid heat dissipation to the metallic substrate. With the coating buildup, the cooling rate becomes smaller because the thermal conductivity of HA ($0.72\text{--}2.16\text{ W m}^{-1}\text{ K}^{-1}$) [28] is much lower than that of metals (in our case, mild steel $\sim 20\text{--}60\text{ W m}^{-1}\text{ K}^{-1}$). Another reason for the decreased cooling rate arises due to the concentration of heat on the substrate during the spray process. The decreased cooling rate and heat accumulation result in more melt recrystallization upon the HA particles striking the substrate and the recrystallization of the amorphous phase in the prior-formed splats; as explained before for the spray power and SOD. This recrystallization process was also accompanied with the re-hydroxylation, as will be shown in the FTIR spectra.

As discussed previously, the crystalline HA in the coating is composed of two parts, i.e. unmelted and recrystallized portions, which cannot be reflected by the crystallinity. These two crystalline components can have different properties, especially when the feedstock is agglomerated particles, as used in this study. So it is necessary to distinguish these two crystalline forms of HA. Some previous references [18,29] have reported that

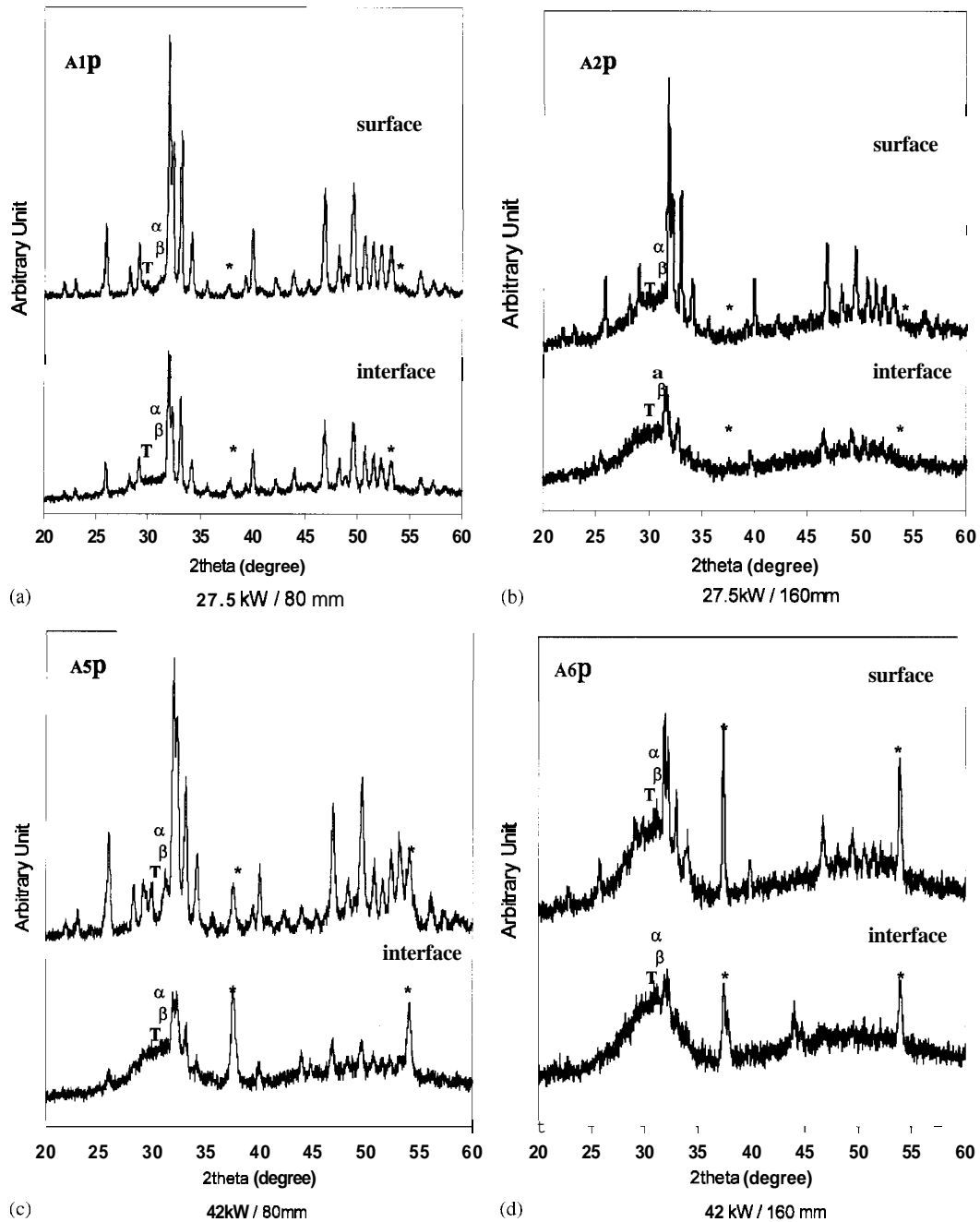


Fig. 4. XRD patterns of the surface and interface of the HA coatings. (a is α -TCP, β is β -TCP, T is TTCP, * is CaO and all other peaks belong to HA).

the recrystallization caused HA peak broadening in the XRD pattern. However, no peak broadening was found in this study after spraying; possibly because the grain size of the feedstock is already very fine.

An estimation of the recrystallization at the coating surface can be made by comparing the difference of the crystallinity at the coating surface and interface. This is based on the fact that the HA particles exhibit similar melting and dehydroxylation states before striking the substrate for the same coating, and only the difference in the solidification and coating buildup processes ac-

counts for the different recrystallization. It is observed that for the two crystalline coatings (A1p and A5p, SOD=80 mm), the crystalline HA of the coating sprayed at higher power (42 kW) is dominated by the recrystallized portion while the coating sprayed at lower power (27.5 kW) is dominated by the unmelted portion. Such responses lead to different microstructures and properties, as will be shown later. The estimation method, however, is very conservative with the assumption that the crystalline HA at the interface arises from the unmelted HA and with no consideration given to the

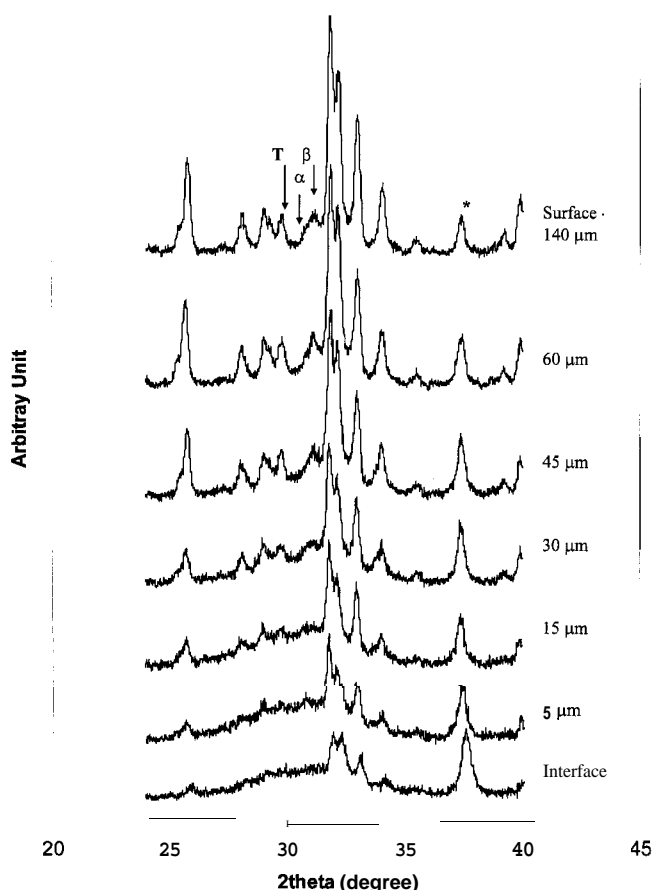


Fig. 5. Phase variation along the thickness of coating A5. (α is α -TCP, β is β -TCP, T is TTCP, * is CaO and all other peaks belong to HA).

impurity phases. The actual recrystallization percentage should be higher since the recrystallization could happen in the first layer of lamellas (at the coating–substrate interface).

3.2. Structural analysis using FTIR

3.2.1. Structural variations with spray parameters

FTIR is another characterization method for HA coatings since it can provide information concerning structural features such as the structural distortion and dehydroxylation state, which cannot be obtained readily using XRD methods. The spectra of HA powders and coatings are shown in Fig. 7. The 961 cm^{-1} band, characteristic of non-degenerate symmetric stretching of the PO_4 group (ν_1) in HA, disappeared in all coatings. The doubly degenerate O–P–O bending band (ν_2) at 434 and 471 cm^{-1} in some references [30,31] were not visible in the spectra of both HA powders and coatings, but there were two weak peaks at 409 and 426 cm^{-1} in the spectra of HA powders. The original asymmetric O–P–O stretching band (ν_3) at 1040 and 1096 cm^{-1} still existed in the coatings, while the splitting of these two bands decreased with the crystallinity of the HA coat-

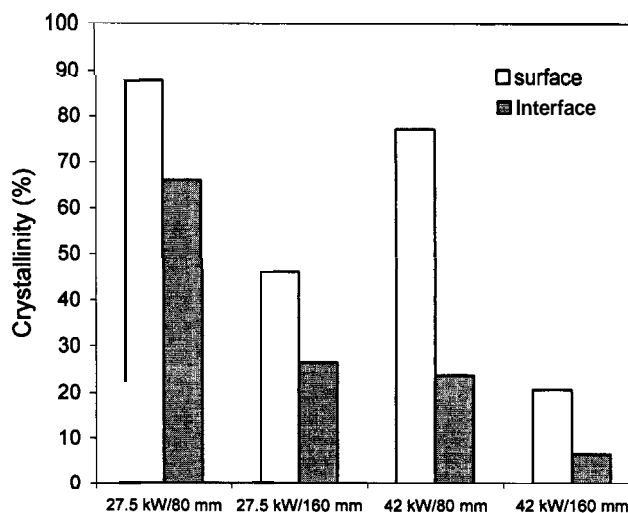


Fig. 6. Comparison of the crystallinity between the surface and interface of the HA coatings (the difference between surface and interface is due to the recrystallization).

ings. The triply degenerate asymmetric O–P–O bending band (ν_4) at 609 and 563 cm^{-1} also existed and their splitting exhibited the same trend with respect to the coating crystallinity, as reported previously [32]. All the structural changes were associated with not only the existence of the ACP phase, but also the distortion of the crystal structure due to dehydroxylation phenomenon.

In addition to PO_4^{3-} groups, the two characteristic OH– bands of HA also changed after spraying. The bending band at 633 cm^{-1} disappeared for all coatings. The stretching band at 3570 cm^{-1} decreased in intensity for the coatings sprayed at 80 mm and almost disappeared for the coatings sprayed at 160 mm . This response is more obvious in the spectra obtained by DRIFT (Fig. 8). As mentioned before, during spraying, the HA was partially dehydroxylated and transformed into OHA [6,17]. Due to the similar structure of HA and OHA, this difference cannot be identified easily by XRD. Therefore, it can be inferred that the previously identified HA by XRD is actually OHA. Hydroxyapatite was subjected to more dehydroxylation at longer SOD; thus, the 3570 cm^{-1} band was almost invisible for the coatings sprayed at 160 mm . X-ray diffraction also indicated that the coatings sprayed at 160 mm were much more amorphous than those sprayed at 80 mm ; therefore, the FTIR results also verified that the amorphous phase has very little (if any) hydroxyl group incorporated within its structure.

In addition to the above two OH– bands, a new OH– band appeared at 3641 cm^{-1} after spraying, which is not derived from the HA structure, but related to the surface $\text{Ca}(\text{OH})_2$ phase [33]. This band is distinct in the spectra of the two coatings sprayed at 42 kW and is consistent with the XRD results since these two

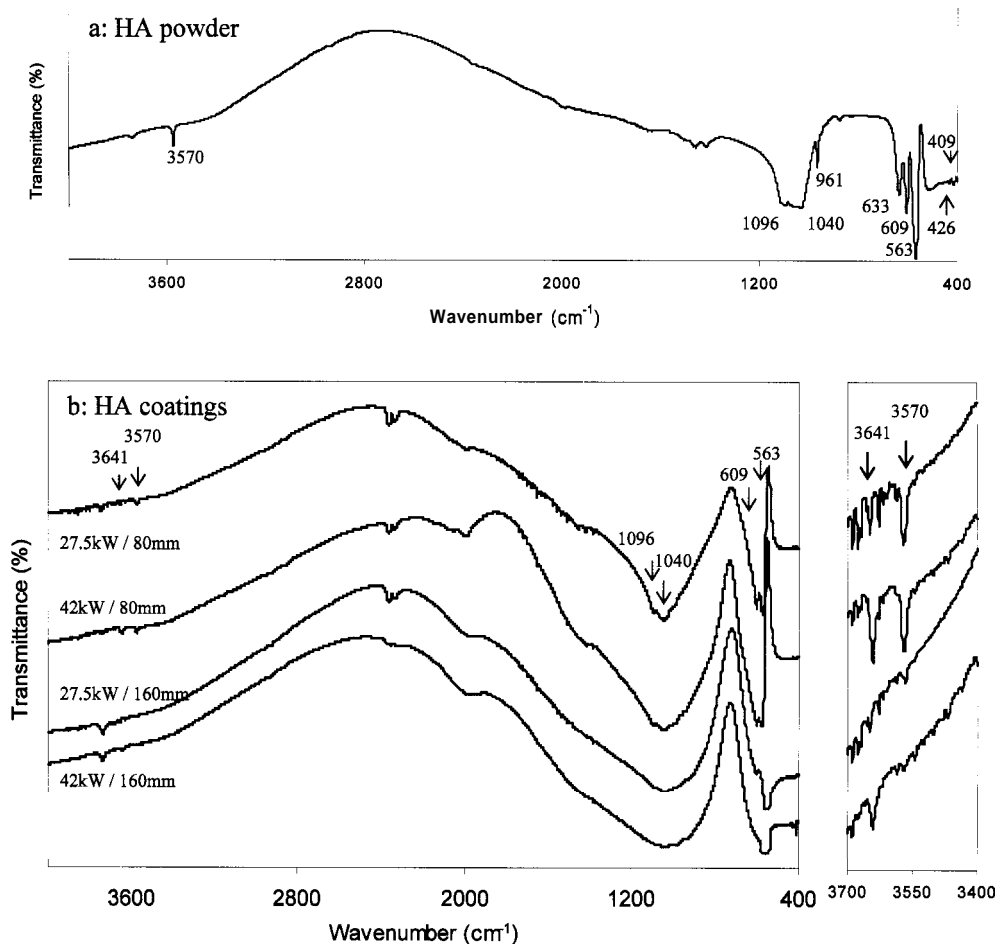


Fig. 7. FTIR spectra of the (a) feedstock HA powders and (b) HA coatings obtained in transmission mode and (c).

coatings demonstrate higher decomposition and CaO contents.

3.2.2. Structural variations in HA coatings

Fig. 8 displays the spectra obtained from the coating surface and interface by DRIFT. As the depth of the IR penetration into the ceramic sample is very small (around several micrometers), the spectra reflect the structure of the near surface and interface of the coatings [31]. The O–H band at 3570 cm^{-1} is smaller for the coating interface than the surface, especially for the two crystalline coatings (SOD = 80 mm). As stated before, the HA particles have similar melting and dehydroxylation states before striking the substrate for the same coating. It can, thus, be deduced that some re-hydroxylation occurred during coating buildup while the initial lower substrate temperature and fast cooling rate could hinder the re-hydroxylation effect. Re-hydroxylation may occur in the areas with heat accumulation in the already formed amorphous phase, which is important for the recrystallization process.

Although fast cooling rate is critical for the formation of amorphous phase, the crystal structure of a material determines if the material will retain the amorphous phase or transform to metastable phases. Hydroxyapatite has a complex structure, and the loss of OH– groups during plasma spraying leads to lattice distortion and vacancies, which makes the diffusion and reconstruction of atoms very difficult. Therefore, amorphous phase is unavoidable in the HA coatings [18] and increased with increasing dehydroxylation. This behavior also suggests that the O–H group is important for the recrystallization of HA and the recrystallization during coating buildup is closely connected to the re-hydroxylation effect.

In addition to the structural OH– band, the OH– band at 3641 cm^{-1} (due to the existence of CaO) is higher for both the surface and interface of the coating sprayed at higher power (42 kW) as a result of higher decomposition. The splitting of the $\text{PO}_4^{3-}\nu_3$ band at 1040 and 1096 cm^{-1} also decreased for the coating interface due to lower crystallinity. These results are all consistent with the XRD results.

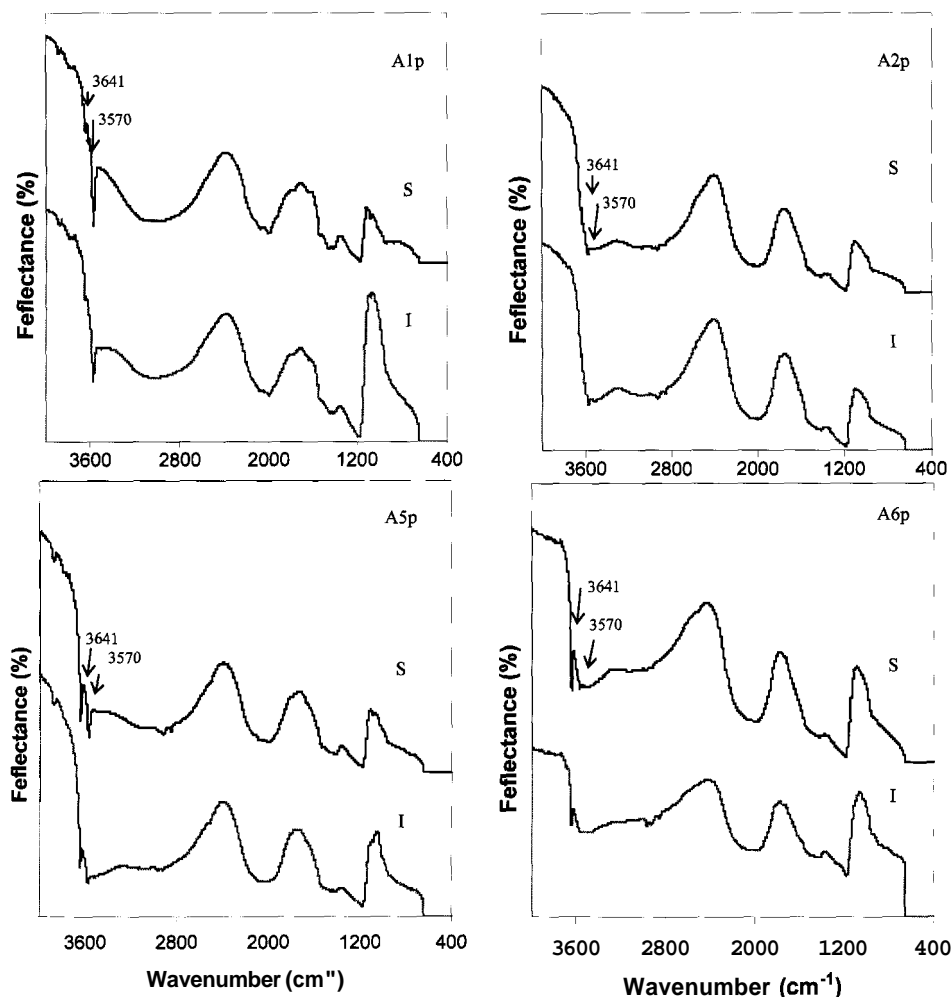


Fig. 8. FTIR patterns of surface (S) and interface (I) of HA coatings.

3.3. Structural analysis using solid state NMR

Solid state NMR spectroscopy was used as another technique to investigate the structure of the HA coating owing to its high sensitivity to the short-range interaction. The ^{31}P spectra were used to determine the position and environment of the phosphate group. Fig. 9 shows the ^{31}P NMR–MAS spectra of the feedstock HA, OHA and four HA coatings. The spectrum of feedstock HA shows only a single sharp line at 1.7 ppm, which corresponds to the equivalence of the phosphate groups in the hexagonal structure of well crystallized HA. In contrast, the spectrum of the OHA exhibits two major peaks at 1.7 and 5.1 ppm and two small peaks at 0.5 and 3.2 ppm, indicating four phosphate environments in the OHA. The difference between the structure of HA and OHA is that linear chains of O–H in HA are replaced by chains of O^{2-} , OH^- and vacancies. Thus, the two lines in OHA may be related to the different distortions of $(\text{PO}_4)^{3-}$ units depending on their positions relative to the ions in the central chains [15].

The spectra of all coatings exhibit two broad overlapping lines (respectively, at ~ 1.7 and ~ 5.1 ppm) with considerably decreased intensity, indicating two dominant phosphorus environments in the coatings. The line broadening in the spectra arises due to the existence of both the amorphous phase and the structural distortion as a result of quenching effects during spraying, and the line width increased with the decrease in the coating crystallinity.

The spectra of the coatings imply that the coating structure is similar to that of OHA by just considering the phosphorus environment; except for the line broadening due to the existence of amorphous phase and structural distortion in the former. This matches the FTIR results. No resonance due to α -TCP (four peaks at 0.5 (58%), 1.8 (20%), 3.3 (12%), 2.2 (9%) ppm, with the numbers in the brackets being the relative peak intensity), β -TCP (three peaks at 0.3 (67%), 4.3 (22%) and 0.5 (11%) ppm) and TTCP (three peaks at 3.2 (50%), 3.1 (42%), and 4.3 (8%) ppm) [34] can be resolved because of the line broadening and overlapping. The line broad-

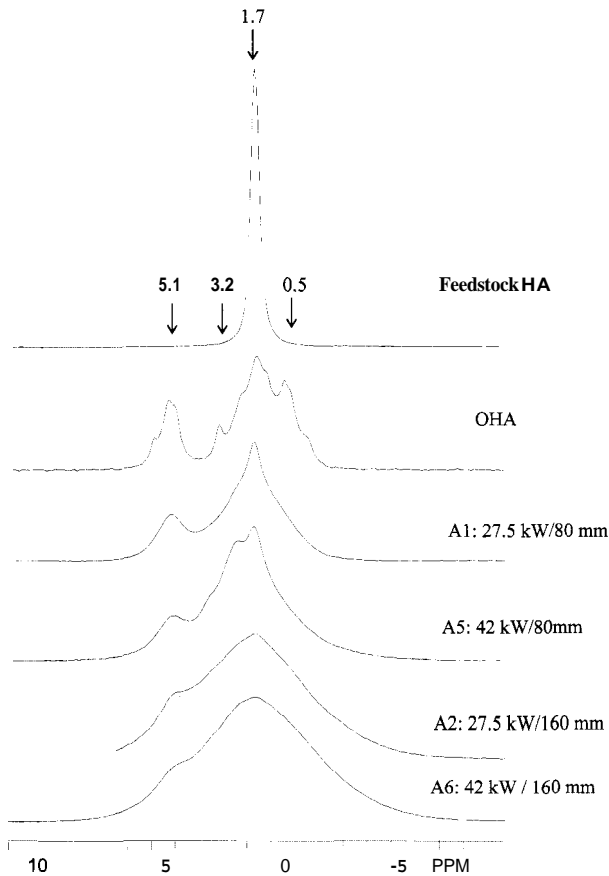


Fig. 9. ^{31}P MAS NMR spectra of the HA coatings

ening effect also renders difficulty for quantitative analysis of the crystal structure of the HA coating, which still requires further investigation.

3.4. Microstructural investigation

The SEM morphology (Fig. 10) of the feedstock HA powders shows that all particles are quite spherical, and each particle is agglomerated by many rod-shaped nano-particles. The size of a single nano-particle is $\sim 50\text{--}200$ nm long with a cross section of $\sim 50 \times 50$ nm 2 .

3.4.1. Surface morphology

Surface morphologies of the coatings are shown in Fig. 11. The morphology of the coating A1 (27.5 kW per 80 mm) was dominated by unmelted and partially melted particles over a small amount of flattened splats. These particles were quite large with a partially melted skin or have been crushed into fine particles that spread on the splats. This result is consistent with the previous XRD results since this coating exhibits the highest crystallinity. Despite the remains of some partially melted particles, the morphology of coating A2 (27.5 kW per 160 mm) was mainly composed of glassy phases including spheroidized particles, accumulated splats and flattened splats due to a longer melting period and rapid

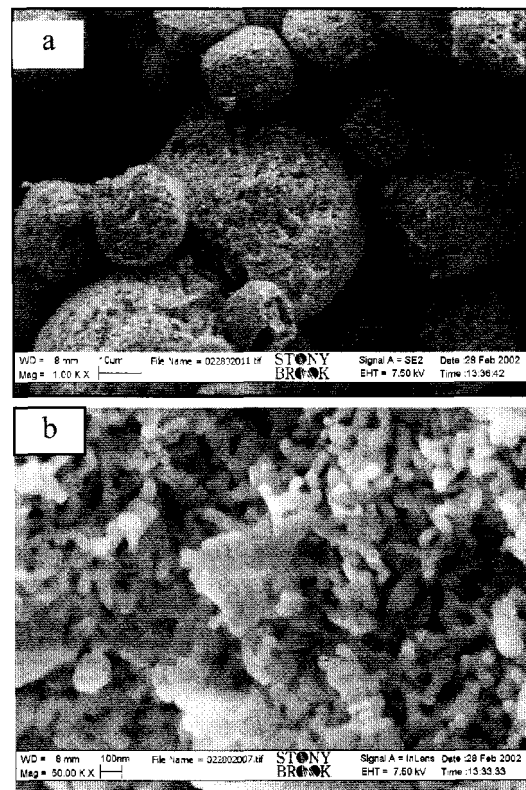


Fig. 10. Morphology (a) and microstructure (b) of the feedstock HA powders.

cooling rate. No large particles existed in this morphology. Such morphological features agree with the explanation for the XRD results presented previously; i.e. some of the unmelted or partially melted particles were de-agglomerated and blown away before they impacted on the substrate at longer SOD. Both coatings A5 and A6 exhibited enhanced particle melting and spreading due to a higher plasma temperature. Coating A5 mainly consisted of flattened and accumulated splats as well as some spheroidized and partially melted particles, while the major characteristics of coating A6 were flattened and accumulated glassy splats and some spheroidized particles. In addition, some pores but no microcracks were observed on the surfaces of the four coatings.

3.4.2. Cross-sectional microstructures

The cross-sectional microstructures of the coatings are shown in Fig. 12. The particles/droplets may be subjected to high densification due to high flame temperature and low surface tension, and subsequent compaction and coalescence upon striking onto the substrate during spraying process; thus the thermal spray coating usually exhibits a lamellar structure. In Fig. 12, no typical lamellar structure can be identified for coating A1 (27.5 kW per 80 mm). Instead, a large amount of pores (porosity is $\sim 12\%$) were distributed throughout the coating matrix. While the small pores

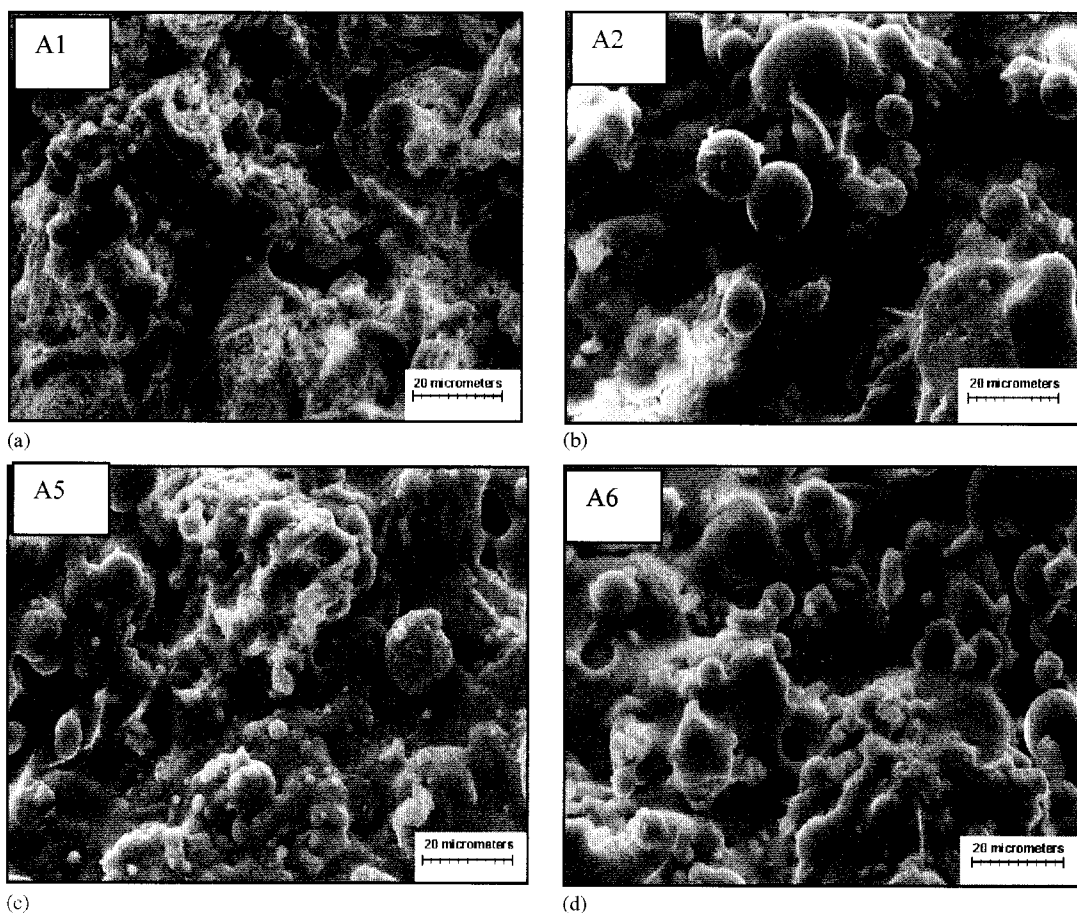


Fig. 11. Surface morphology of the HA coatings (a) A1: 27.5 kW 80 mm, (b) A2: 27.5 kW 160 mm, (c) A5: 42 kW 80 mm, (d) A6: 42 kW 160 mm.

were produced during spraying due to solidification contraction and splat filling effects, the large pores represent the pullouts of unmelted particle cores during the grinding and polishing process. Very few cracks were observed for this coating. The microstructure as viewed by optical microscopy (Fig. 12b) shows the partially melted particles (with a melted shell and an unmelted core, as indicated by the arrow) embedded in the coating structure.

Coating A5 (42 kW per 80 mm) exhibited the typical lamellar structure, with thin layer thickness and obvious splat boundaries (Fig. 12). As known before, this coating underwent high melting and recrystallization; therefore, the contraction from the recrystallization process resulted in the distinct splat boundary. The porosity level in this coating ($\sim 7\%$) is much lower compared to coating A1 as a result of much better melting, and the pores are usually small due to splat filling effects. However, many microcracks were observed, mostly perpendicular to the coating–substrate interface, indicating high tensile stress along the coating–substrate interface direction in the coating during the cooling. These microcracks were produced during either the spraying or sample polishing processes.

Longer SOD usually reduces the velocity of the droplets during spraying due to the frictional forces from air molecules, which results in less spreading when the droplets strike onto the substrate. However, as indicated before, the two coatings sprayed at 160 mm SOD (A2 and A6) were mainly composed of amorphous phase. Amorphous coatings usually result from much better melting during spraying, and thus better spreading upon solidification compared with the unmelted portion. As well, unlike its crystalline counterpart, amorphous phase does not have a distinct melting point, but exhibits a glass transition temperature range. Therefore, amorphous phase can exhibit a viscous flow at temperatures much lower than the melting point of its crystalline counterpart. This helps fill the pores and voids between neighboring splats. Therefore, these two coatings exhibit a more smooth and glassy microstructure without obvious splat boundaries (Fig. 12). The porosity levels in these two coatings ($\sim 5\%$ for coating A6 and $\sim 3\%$ for coating A2, respectively) are even lower than in coating A5, and there are also some microcracks observed.

Another microstructural feature is also shown clearly in Fig. 12; i.e. some ribbon-like regions exist throughout

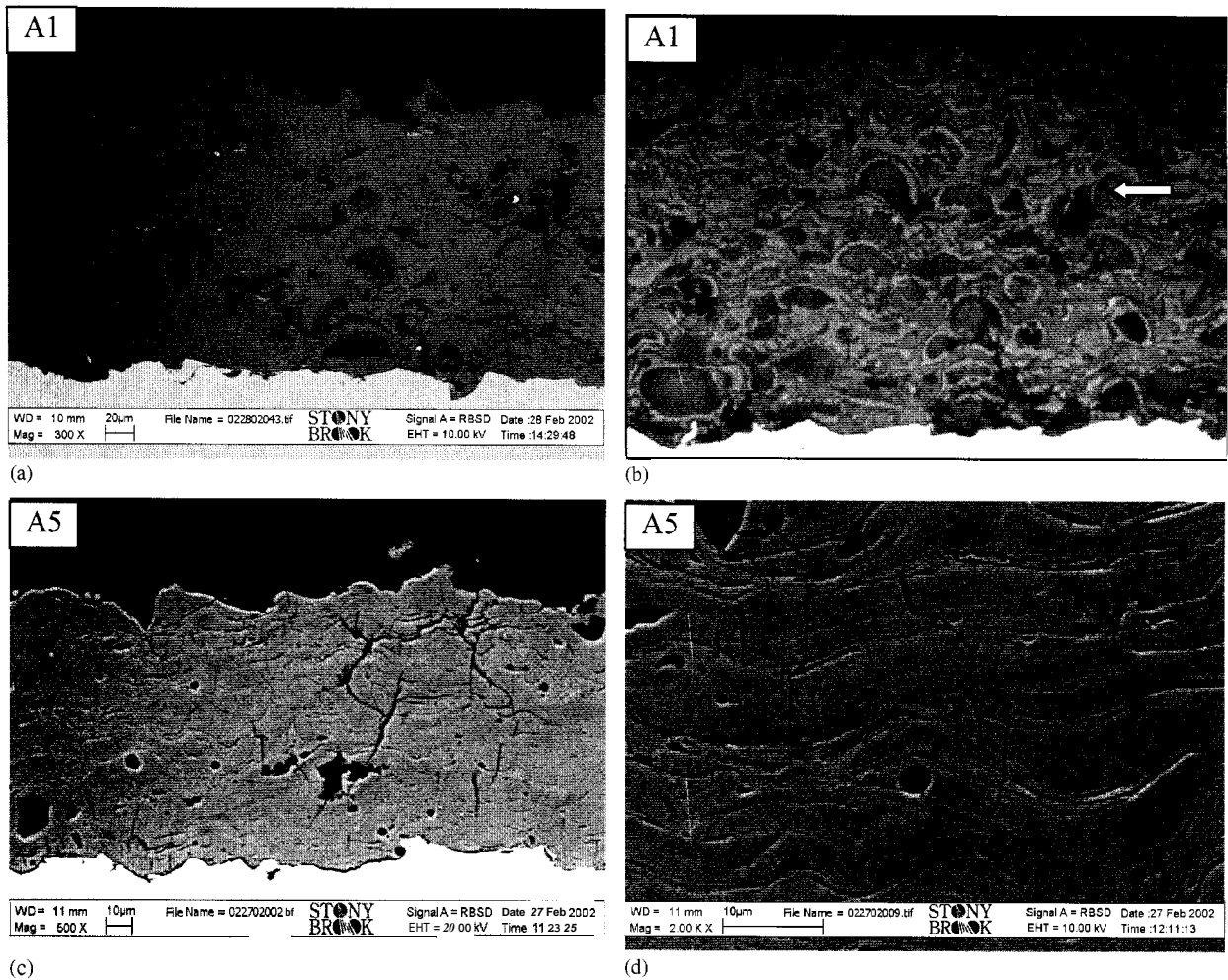


Fig. 12. Microstructure of the cross-section of the HA coatings by SEM. (a, b) A1: 27.5 kW 80 mm, (c, d) A2: 27.5 kW 160 mm, (e, f) A5: 42 kW 80 mm, (g, h) A6: 42 kW 160 mm.

the coating in coating A6 (smaller amounts in coating A2, too). A high magnification (Fig. 13) image shows that these regions exhibit a quite different microstructure from the surrounding smooth regions and the boundary between these two regions is smooth. The ribbon-like regions are composed of many granular nano-grains with a particle size of a few to ~ 30 nm; much less than the size of nanoparticles in the feedstock powders. Further investigation found that this ribbon-like region was not significant in coating A1, but was predominant in coating A5 (Fig. 13), which was blurred by the splat-boundary under lower magnification. However, the boundary between the ribbon-like regions and the surrounding regions are coarse in coating A5. This difference may be due to the fact that coating A5 is much more crystalline than coating A6. A similar microstructure has been reported previously, and the ribbon-like regions were found to be crystalline calcium phosphate phase and have a Young's modulus of sintered HA [8]. Thus, most possibly, these regions are newly recrystallized HA grains. But it is difficult to

establish whether the recrystallization occurred from the melt directly or from the amorphous phase, which still needs further investigation. Nanostructured ceramics have been shown to have better wear, impact and toughness properties than the traditional micrograined materials. As well, the dissolution of the HA nanocrystals may become higher compared with well crystallized HA due to the higher volume of the interface, imperfections and higher internal energy. These are all important for the HA as biomedical coatings. Thus, it is expected that the above nanostructure will affect the mechanical, chemical and physiological properties of the HA coatings.

4. Microhardness

The difference in the phase, structure and microstructure is expected to lead to different dissolution behavior and mechanical properties of the coatings. The effects on the dissolution behavior have been discussed

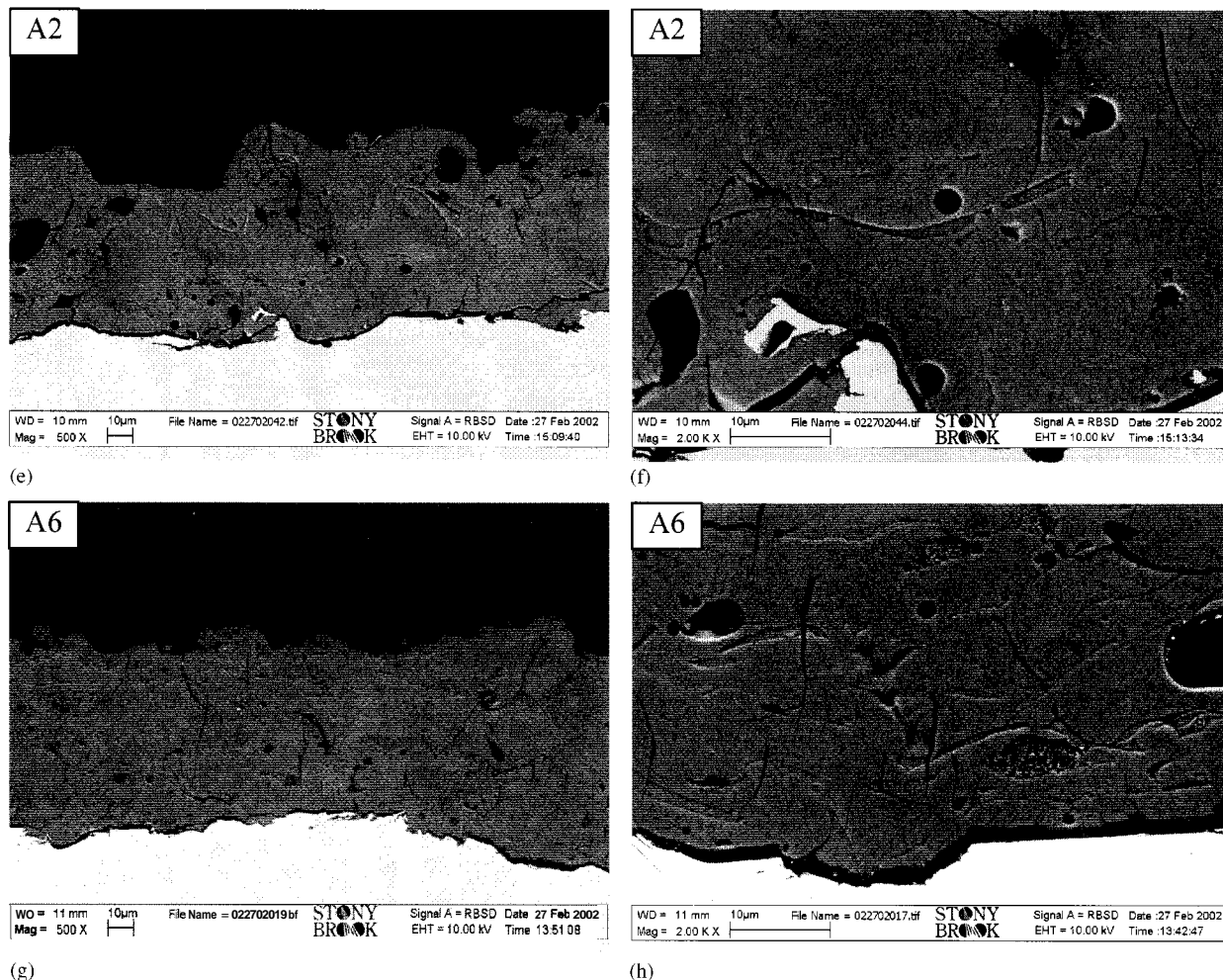


Fig. 12 (Continued)

in a previous work [35], which indicated that the dissolution of the HA coating was not only affected by the crystallinity, but also by the dehydroxylation and recrystallization states in the coatings. The microhardness of the coatings, Fig. 14, does not exhibit any simple relationship with either the crystallinity or the porosity of the coatings. Actually, both these two factors should be considered together with the components of the crystalline HA phase and other microstructural features existed in the coating. The diagonal length of the indent was between 13 and 24 μm , which have included most of microstructural features mentioned above and can reflect the overall properties of the coatings.

The coatings sprayed at higher power levels (A5 and A6) exhibited better particle melting and spreading as well as recrystallization; thus, these two coatings have much higher microhardness. The presence of porosity and amorphous phase usually leads to lower hardness. When comparing two coatings sprayed at the same power but different SOD, these two factors usually contradict; i.e. the coatings sprayed at longer SOD have higher contents of amorphous phase but lower porosity.

Therefore, the resulting microhardness depends on the balance of these two factors. Also the coatings sprayed at lower power and shorter SOD (A1) exhibit the poorest melting status and highest porosity ($\sim 12\%$); which also correlates well with the lowest microhardness.

5. Summary

The current work has concentrated on the HA coatings sprayed under four extreme spray power/SOD combinations. This focus is important because many processing parameters are incorporated during the spray process. An experimental design including all parameters is complex and unnecessary since their effects can generally be attributed to the temperature–time experiences of the feedstock powders, their cooling rate and rehydroxylation/recrystallization process during coating buildup. Since the crystallinity alone cannot reflect the coating quality, this work has emphasized the effects of spray parameters on the chemical structure

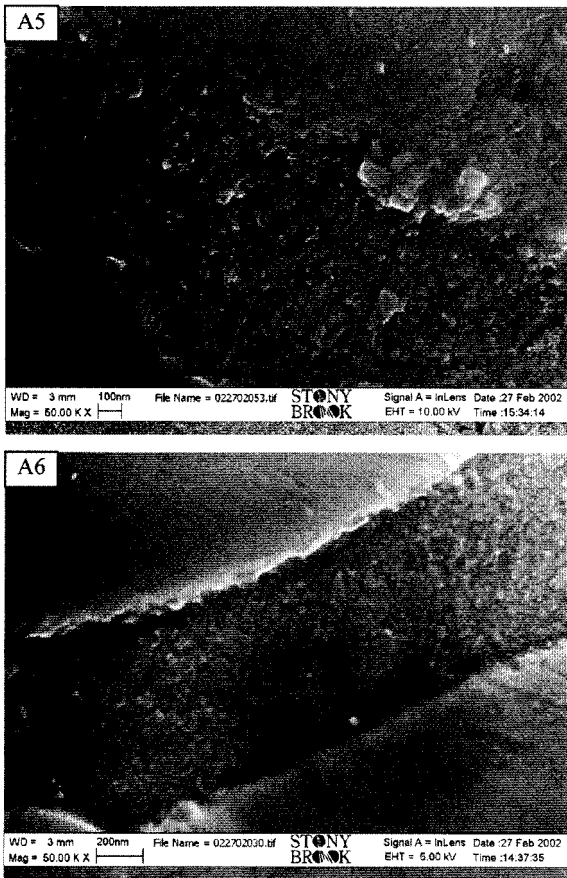


Fig. 13. Microstructure of the ribbon-like regions in coating A5 (42 kW 80 mm) and coating A6 (42 kW 160 mm).

and microstructure of the coatings. As different spray parameters sometimes conflict with each other, a balance shall be reached to obtain an optimal design. In addition, some techniques shall be considered. For example, the substrate temperature can be increased to promote recrystallization for the initial few layers of the coating; and water vapor can be induced around the substrate to prevent the dehydroxylation of the powder or promote re-hydroxylation the droplets. To gain a better understanding of the fundamentals of the deposition and coating buildup processes for the HA coating, further systematic studies of various parameters on the splat morphology, microstructure, phase, hydroxyl state can be suggested.

6. Conclusions

- Hydroxyapatite coatings demonstrate different composition and structure from those of feedstock HA. Both the crystallinity and purity of HA decreased after spraying. XRD revealed the presence of crystalline HA, ACP and impurities including α -TCP, β -TCP, TTCP, and CaO. FTIR and NMR reflected the

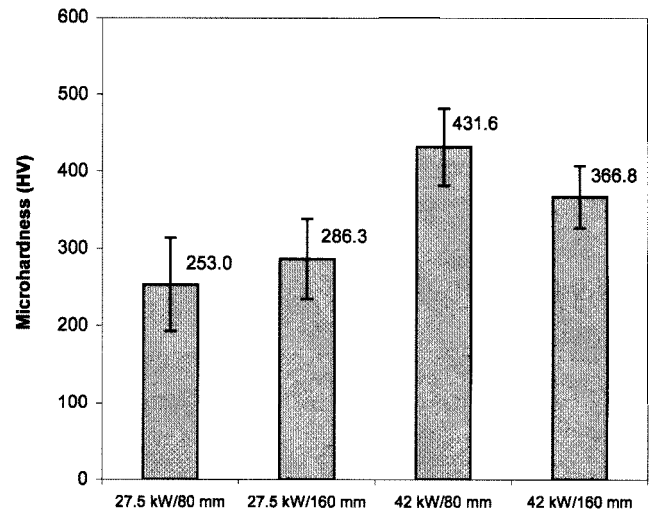


Fig. 14. Microhardness of the HA coatings

changes of both hydroxyl and phosphate and implied that the HA identified by XRD was actually OHA.

- Phase and structure of the HA coatings varied with respect to the spray parameters and locations. Crystallinity and hydroxyl contents of HA coatings decreased with increasing spray power and SOD, and increased from the coating interface to surface. Impurity phase content increased with the increasing power.
- Crystallinity alone cannot reflect coating quality due to the existence of various HA structures; i.e. unmelted, recrystallized and dehydroxylated (OHA), and the gradient coating structure.
- The phase and structural effects were related to particle melting, dehydroxylation, cooling rate, recrystallization and re-hydroxylation, and deposition efficiency in the plasma spray process.
- Surface morphology and the cross-sectional microstructure of the HA coatings sprayed at higher power and longer SOD reveals enhanced particle melting and spreading, lower porosity and more microcracks.
- HA coatings sprayed under different parameters show distinct microstructures: (i) a very porous microstructure for coatings with least melting, (ii) a glassy microstructure with no obvious splat boundary for amorphous coatings, and (iii) a typical lamellar structure for coatings with high recrystallization. High magnification SEM revealed the existence of some newly formed nanocrystalline regions within the coating, which may affect mechanical, chemical and physiological properties of the HA coatings.
- The microhardness of the HA coatings was determined by several microstructural factors; i.e. the particle melting, recrystallization, and volume of amorphous phase and porosity.

Acknowledgements

The authors would like to thank Namjun Kim and Haiming Liu in Chemistry Department for their help with the Nuclear Magnetic Resonance (NMR) experiments.

References

- [1] C.C. Berndt, G.N. Haddad, A.J.D. Farmer, K.A. Gross, *Mater. Forum* 14 (1990) 161–173.
- [2] Y.C. Tsui, C. Doyle, T.W. Clyne, *Biomaterials* 19 (1998) 2015–2029.
- [3] W.D. Capello, J.A. D'Antonio, J.R. Feinberg, M.T. Manley, *J. Bone Jt. Surg.* 79-A (7) (1997) 1023–1029.
- [4] B.C. Wang, E. Chang, T.M. Lee, C.Y. Yang, *J. Biomed. Mater. Res.* 29 (1995) 1483–1492.
- [5] K.A. Gross, C.C. Berndt, Optimization of spraying parameters for hydroxyapatite, in: S. Blum-Sandmeier, H. Eschnauer, P. Huber (Eds.), *Proceedings of Second Plasma-Technik Symposium*, vol. 3, Plasma-Technik AG, Wohlen, Switzerland, 1991, pp. 159–170.
- [6] S.R. Radin, P. Ducheyne, *J. Mater. Sci. Mater. Med.* 3 (1992) 33–42.
- [7] R.Z. LeGeros, *Clin. Mater.* 14 (1993) 65–68.
- [8] J. Wen, Y. Leng, J.Y. Chen, C. Zhang, *Biomaterials* 21 (2000) 1339–1343.
- [9] S.H. Maxian, J.P. Zawadsky, M.G. Dunn, *J. Biomed. Mater. Res.* 27 (1993) 111–117.
- [10] B.C. Wang, T.M. Lee, E. Chang, C.Y. Yang, G.L. Chang, *J. Biomed. Mater. Res.* 36 (1997) 39–48.
- [11] S.W.K. Kweh, K.A. Khor, P. Cheang, *J. Mater. Process. Tech.* 89–90 (1999) 373–377.
- [12] K.A. Khor, P. Cheang, *J. Thermal Spray Tech.* 5 (1996) 310–316.
- [13] J.P. LeGeros, R.Z. LeGeros, A. Burgess, B. Edwards, J. Zitelli, X-ray diffraction method for the quantitative characterization of calcium phosphate coatings, in: E. Horowitz, J.E. Parr (Eds.), *Characterization and Performance of Calcium Phosphate Coatings for Implant*, ASTM STP 1196, ASTM, Philadelphia, PA, 1994, pp. 33–42.
- [14] B.C. Wang, E. Chang, T.M. Lee, C.Y. Yang, *J. Biomed. Mater. Res.* 29 (1995) 1483–1492.
- [15] R. McPherson, N. Gane, *J. Mater. Sci. Mater. Med.* 6 (1995) 327–334.
- [16] J.C. Trombe, G. Montel, *J. Inorg. Nucl. Chem.* 40 (1978) 15–21.
- [17] W. Van Raemdonck, P. Ducheyne, P. De Meester, Calcium phosphate ceramics, in: P. Ducheyne, W. Hasting (Eds.), *Metal and Ceramic Biomaterials*, vol. 2, CRC Press, Boca Raton, FL, 1984, p. 149.
- [18] J. Weng, X. Liu, X. Li, X. Zhang, *Biomaterials* 16 (1995) 39–44.
- [19] K.A. Gross, C.C. Berndt, H. Herman, *J. Biomed. Mater. Res.* 39 (1998) 407–414.
- [20] P.V. Riboud, *Ann. Chim.* 8 (1973) 381–390.
- [21] K. de Groot, C.P.A.T. Klein, J.G.C. Wolke, J.M.A. de Blicke-Hogervorst, Plasma-sprayed coatings of calcium phosphate, in: T. Yamamuro, L.L. Hench, J. Wilson (Eds.), *CRC Handbook of Bioactive Ceramics*, CRC Press, Boca Raton, MA, 1990, pp. 3–16.
- [22] C.Y. Yang, B.C. Wang, E. Chang, J.D. Wu, *J. Mater. Sci. Mater. Med.* 6 (1995) 249–257.
- [23] L. Sun, C.C. Berndt, R.S. Lima, A. Kucuk, K.A. Khor, Effects of spraying parameters on phase formation and distribution in plasma sprayed hydroxyapatite coatings, in: C.C. Berndt (Ed.), *Proceedings of International Thermal Spray Conference—ITSC*, May 8–11, 2000, Montreal, Canada, ASM International, Materials Park, OH, 2000, pp. 803–811.
- [24] K.A. Gross, The amorphous phases in hydroxyapatite coatings, Ph.D. dissertation, State University of New York at Stony Brook, Stony Brook, NY, 1996, p. 175.
- [25] K.A. Khor, P. Cheang, Characterization of plasma sprayed hydroxyapatite powders and coatings, in: C.C. Berndt, T.F. Bernecki (Eds.), *Thermal Spray Coatings: Research, Design and Applications*, ASM International, Ohio, 1993, pp. 347–352.
- [26] C.R.C. Lima, R. da Exaltacao Trevisan, *J. Thermal Spray Tech.* 8 (2) (1999) 323–332.
- [27] H. Ji, C.B. Ponton, P.M. Marquis, *J. Mater. Sci. Mater. Med.* 3 (1992) 283–287.
- [28] T.W. Clyne, Y.C. Tsui, The effect of intermediate layers on residual stress distributions and debonding of sprayed thermal barrier coatings, in: B. Ilschner (Ed.), *Third International Symposium on Structural and Functional Gradient Materials*, PPUR, 1994, pp. 129–136.
- [29] B. Koch, J.G.C. Wolke, K. de Groot, *J. Biomed. Mater. Res.* 24 (1990) 655–667.
- [30] S.R. Levitt, The vibrational spectroscopy and normal coordinate analysis of geological apatites, Ph.D. thesis, Alfred University, Alfred, New York, 1969.
- [31] E. Park, R.A. Condrate, Sr, D. Lee, *Mater. Lett.* 36 (1998) 38–43.
- [32] J.D. Termine, A.S. Posner, *Nature* 211 (1996) 268–270.
- [33] A. Slosarczyk, C. Paluszkiwicz, M. Gawlicki, Z. Paszkiewicz, *Ceram. Int.* 23 (1997) 297–304.
- [34] J. Vogel, C. Russel, G. Gunther, P. Hartmann, F. Vizethum, N. Bergner, *J. Mater. Sci. Mater. Med.* 7 (1996) 495–499.
- [35] L. Sun, C.C. Berndt, K.A. Khor, P.N. Cheang, K.A. Gross, *J. Biomed. Mater. Res.* 62 (2) (2002) 228–236.